

len in situ, either chemically or photochemically, thereby releasing the contents.

Colloidosomes can address a wide variety of encapsulation needs in addition to nutrient and drug delivery. One important possibility is immunoisolation of living cells by encapsulation in colloidosomes; they would provide a rigid scaffold that supports the living cell while simultaneously protecting it from the immune system and allowing free diffusion of gases and nutrients (1, 3, 35). The required 25-nm pore diameter would be achieved using colloidal spheres of 170-nm diameter, well within the range of sizes of particles known to adsorb strongly onto droplets. Colloidosomes encapsulating cells could also have advantageous properties as bioreactors (8, 36). Furthermore, a superstructure of colloidosomes may form templates for tissue growth by providing a protected environment that has a useful three-dimensional architecture and allows rapid permeation of small macromolecules. In preliminary experiments, we successfully encapsulated living fibroblast cells and maintained their viability for several hours using particle-coated water droplets in decalin oil. In many cases, the cells adhered to the solid surfaces, suggesting that colloidosomes can be fabricated as rigid porous superstructures to enhance the viability of the cells. Plant protoplast cells are known to survive and grow even after 25 days in contact with oxygen-perfused perfluorodecalin oil, suggesting that the exterior oil phase might not damage the cells during a brief exposure (37). The key to cell viability is the suitability of the colloidosomes surface; other methods of locking the particles together, such as avidin-biotin binding, may make the colloidosomes even more biocompatible.

Colloidosomes successfully meet many of the key requirements for encapsulation: Emulsification provides a simple means of producing capsules from a wide variety of fluids and with controlled sizes ranging from submicrometer to several millimeters (38, 39). Furthermore, because the internal and external fluids remain completely separate until the final step, materials can be encapsulated efficiently with minimal loss. The choice of different colloidal particles allows for additional flexibility. We show that the permeability and rupture stress of the capsules can be controlled through the size of the coating particles and through postfabrication treatment by sintering or, alternatively, by further filling of the holes with smaller particles or polymers. A variety of release strategies may be feasible, either through control of their permeability for slow but sustained release, or through control of their rupture stress for shear-induced breakup. This flexibility will allow a wide range of potential applications to be explored.

References and Notes

1. E. L. Chaikof, *Annu. Rev. Biomed. Eng.* **1**, 103 (1999).
 2. B. F. Gibbs, S. Kermasha, I. Alli, C. N. Mulligan, *Int. J. Food Sci. Nutr.* **50**, 213 (May 1999).

3. R. P. Lanza, R. Langer, J. Vacanti, *Principles of Tissue Engineering* (Academic Press, San Diego, CA, 2000).
 4. T.-A. Read et al., *Nature Biotechnol.* **19**, 29 (2001).
 5. T. Joki et al., *Nature Biotechnol.* **19**, 35 (2001).
 6. I. Cohen, H. Li, J. L. Houglund, M. Mrksich, S. R. Nagel, *Science* **292**, 265 (2001).
 7. I. G. Loscertales et al., *Science* **295**, 1695 (2002).
 8. R. G. Willaert, G. V. Baron, *Rev. Chem. Eng.* **12**, 5 (1996).
 9. F. Lim, A. M. Sun, *Science* **210**, 908 (1980).
 10. G. Decher, *Science* **277**, 1232 (1997).
 11. F. Caruso, R. A. Caruso, H. Möhwald, *Science* **282**, 1111 (1998).
 12. F. Tiarks, K. Landfester, M. Antonietti, *Langmuir* **17**, 908 (2001).
 13. S. M. Marinakos et al., *J. Am. Chem. Soc.* **121**, 8518 (1999).
 14. F. Caruso, W. Yang, D. Trau, R. Renneberg, *Langmuir* **16**, 8932 (2000).
 15. G. B. Sukhorokov, M. Brumen, E. Donath, H. Möhwald, *J. Phys. Chem. B* **103**, 6434 (1999).
 16. O. D. Velev, K. Furusawa, K. Nagayama, *Langmuir* **12**, 2374 (1996).
 17. ———, *Langmuir* **12**, 2385 (1996).
 18. O. D. Velev, K. Nagayama, *Langmuir* **13**, 1856 (1997).
 19. T. A. Desai, D. J. Hansford, M. Ferrari, *Biomol. Eng.* **17**, 23 (2000).
 20. P. A. Kralchevsky, K. Nagayama, *Adv. Colloid Interface Sci.* **85**, 145 (2000).
 21. B. P. Binks, J. H. Clint, *Langmuir* **18**, 1270 (2002).
 22. Y. Lin, H. Skaff, T. S. Emrick, A. D. Dinsmore, T. P. Russell, unpublished data.
 23. P. Pieranski, *Phys. Rev. Lett.* **45**, 569 (1980).
 24. G. Y. Onoda, *Phys. Rev. Lett.* **55**, 226 (1985).
 25. M. G. Nikolaidis et al., *Nature*, in press.
 26. M. J. Bowick, D. R. Nelson, A. Travesset, *Phys. Rev. B* **62**, 8738 (2000).
 27. A. R. Bausch et al., unpublished data.
 28. P. N. Pusey, W. van Meegen, *Nature* **320**, 340 (1986).
 29. Materials and Methods are available as supporting material on Science Online.
 30. A. J. Hurd, *J. Phys. A* **18**, L1055 (1985).
 31. O. D. Velev, A. M. Lenhoff, E. W. Kaler, *Science* **287**, 2240 (2000).
 32. V. Gordon, D. A. Weitz, unpublished data.
 33. H. C. Berg, *Random Walks in Biology* (Princeton Univ. Press, Princeton, NJ, 1993).
 34. B. E. Rodriguez, M. S. Wolfe, M. Fryd, *Macromolecules* **27**, 6642 (1994).
 35. L. Leoni, T. A. Desai, *IEEE Trans. Biomed. Eng.* **48**, 1335 (Nov. 2001).
 36. J. K. Park, H. N. Chang, *Biotechnol. Adv.* **18**, 303 (2000).
 37. K. C. Lowe, P. Anthony, M. R. Davey, J. B. Power, *Artif. Cells Blood Subst. Immobil. Biotechnol.* **27**, 255 (1999).
 38. P. B. Umbanhowar, V. Prasad, D. A. Weitz, *Langmuir* **16**, 347 (2000).
 39. A. M. Ganan-Calvo, J. M. Gordillo, *Phys. Rev. Lett.* **87**, 4501 (2001).
 40. We gratefully acknowledge valuable conversations with V. Gordon, D. Nelson, and A. Akashe. We also thank A. Schofield for the PMMA particles. We also gratefully acknowledge support from Kraft. This work was also supported by the NSF (DMR-9971432) the Harvard Materials Research Science and Engineering Center (DMR-9809363) and NASA (NAG3-2284). A.B. acknowledges support from the Emmy Noether-Programme of the DFG.

Supporting Online Material

www.sciencemag.org/cgi/content/full/298/5595/1006/DC1

Materials and Methods
 Figs. S1 and S2

10 June 2002; accepted 1 October 2002

Detection and Monitoring of Ongoing Aseismic Slip in the Tokai Region, Central Japan

Shinzaburo Ozawa,* Makoto Murakami, Masaru Kaidzu, Takashi Tada, Takeshi Sagiya, Yuki Hatanaka, Hiroshi Yarai, Takuya Nishimura

Analysis of global positioning system data shows that the rate of crustal deformations in the Tokai region of Japan, a seismic gap area, changed over the past 18 months. Kalman filtering analysis shows aseismic slip on the plate boundary in the western Tokai region centered on Lake Hamana, adjacent to the anticipated Tokai earthquake source area. The cumulative moment magnitude reaches 6.7 in June 2002 with a relative slip increase northeast of Lake Hamana from January 2002. An existence of aseismic slip in the western Tokai supports the hypothesis of a silent event as the cause of uplifting several days before the 1944 Tonankai earthquake.

The Tokai region is located along the Pacific coast of central Japan about 200 km to the southwest of Tokyo. The Suruga trough, a subduction plate boundary between the Eurasian plate and the Philippine Sea plate, runs just off the shore of this area (Fig. 1). In this

tectonic setting, the Tokai area has experienced large offshore earthquakes with time intervals of around 150 years. Since the 1854 Tokai earthquake, Richter magnitude $M = 8.4$, the Tokai region has been loaded by the Philippine Sea plate and did not rupture at the time of the 1944 Tonankai earthquake (moment magnitude $M_w = 8.1$) (1–3). Continuous global p system (GPS) data since 1994 and historical geodetic survey data by the Geographical Survey Institute of Japan (GSI) for about 100 years indicate a steady strain

Geography and Crustal Dynamics Research Center, Geographical Survey Institute of Japan, Kitasato-1, Tsukuba, Ibaraki, Japan, 305-0013.

*To whom correspondence should be addressed. E-mail: ozawa@gsi.go.jp

accumulation in this region (3, 4). On the basis of these pieces of evidence, the Tokai region has been regarded as a seismic gap with a potential of $M_w = 8$ earthquake.

A large seismo-volcanic event occurred in the Izu islands from July to September 2000 (5, 6), causing southeastward horizontal displacements in the Tokai and northeastward displacements in the Kanto region, central Japan, in a range of up to 3 cm from the dike opening and fault creeping caused by magma intrusion in the Izu Islands (5). After October 2000, the effect of the Izu islands activity faded and the Tokai and Kanto regions returned approximately to the previous normal state of crustal deformation for the period between 1997 and 1999, when displacement rates were almost constant (Fig. 1B). However, another stage of surface displacements gradually became evident in the Tokai region at the beginning of 2001 in the GPS time series.

By subtracting the estimated linear and annual components (7), we detrended the raw time series for the period between April 1996 and June 2002. The detrended time series of selected GPS sites indicates that ground motion started to change in January 2001 (Fig. 2). The spatial pattern of the observed anomalous ground motion for the period between January 2001 and June 2002 (Fig. 3A) indicates southeastward motion of around 2 cm at stations 054, 096, 097, and 098 in the western Tokai region. Because of the steady northwestward motion observed during 1997–1999 (Fig. 1B), the post-2001 data suggests the possibility of aseismic slip between the Philippine Sea plate and the overriding Eurasian plate in the western Tokai region during 2001–2002. Maximum uplift of 2 cm is observed at station 054 east of Lake Hamana where the maximum horizontal motions occur. Crustal deformation on the Izu islands (Fig. 3A) shows a continuation of the 2000 Izu islands event with much less intensity than the peak period between July and August 2000. Southeastward surface displacements on the Izu peninsula are mostly attributed to the Izu islands activity because displacements in the same direction were observed during the 2000 Izu islands event (5).

On the assumption that aseismic slip is causing the abnormal crustal deformation in the Tokai, we estimated the slip history between the Philippine Sea plate and the overriding plate by a Kalman filter–based analytical method (8, 9) analogous to the time-dependent inversion method (10, 11) using the data in Figs. 2 and 3, with the 2000 Izu islands activity taken into account (12). We used east-west, north-south, and up-down displacement data at 99 selected GPS sites (Fig. 3B) on the Izu island chain and in the Kanto and Tokai regions. As a model region, we use the plate boundary estimated by

Ishida (13) and the 2000 Izu islands model (12) (Fig. 4). Adopting these model regions represented by spline surfaces (8), we estimated the slip history between September 2000 and June 2002. We set slip components at zero at the edge of the fault patch as a boundary condition. Furthermore we adopted the condition that the slip motion is southward and eastward for the Tokai aseismic slip.

Our analysis for the Tokai aseismic slip gives an area of slip around the Lake Hamana, western Tokai region, close to the estimated Tokai seismic gap (4, 14) (Fig. 1B) from October 2000, which spread slightly through July 2001 (Fig. 4). We think that

aseismic slip infiltrating the Tokai earthquake source region is very small and within uncertainties of the identified source area and our model. From November 2001, the estimated slip magnitude decreased near Lake Hamana and a relative slip increase is observed northeast of Lake Hamana (Fig. 4). Slip motion occurs from October 2000 and slows down from November 2001 at point 1, whereas point 2 shows aseismic slip starting after point 1 and the amount of motion nears that at point 1 in 2002 (Fig. 4 and fig. S1). The time evolution of moment released from the estimated Tokai interplate aseismic slip starts in October 2000, increases linearly until July 2001, and continues with a slightly decreased

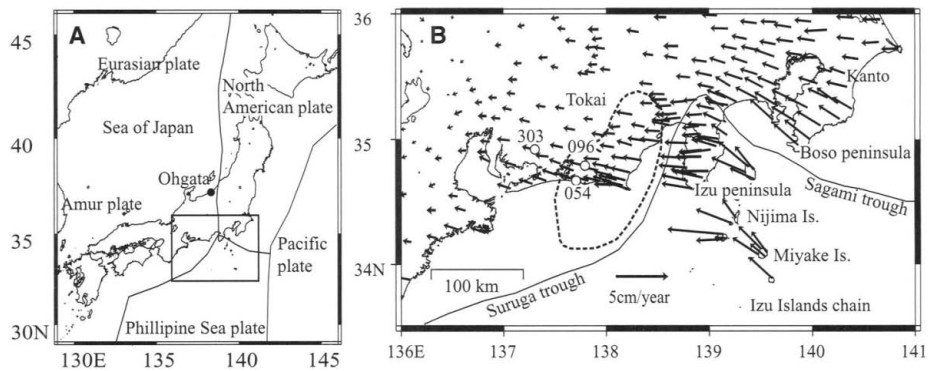


Fig. 1. (A) Tectonic setting in and around Japan. The solid lines indicate plate boundaries. Solid circle shows the location of Ohgata GPS site. (B) Magnified map of a rectangular area in (A). The Philippine Sea plate subducts under the Eurasian plate from the Suruga and Sagami troughs. The black arrow at bottom represents the observed ground displacement rate in cm/year for the period between 1997 and 1999 relative to Ohgata station (Fig. 1A). Northwestward motions (small arrows) in the Kanto and Tokai regions are mainly due to the coupling effect between the subducting Philippine Sea plate and the overriding Eurasian plate. This crustal deformation is referred as the steady deformation. Dashed line represents the source area of the future Tokai earthquake adopted by the Central Disaster Management Council of the Japanese government on the basis of many proposed models that were constrained using crustal deformation, seismicity, or other available data [e.g. (4, 14)]. The open circles show the location of the selected GPS stations whose time series are shown in Fig. 2.

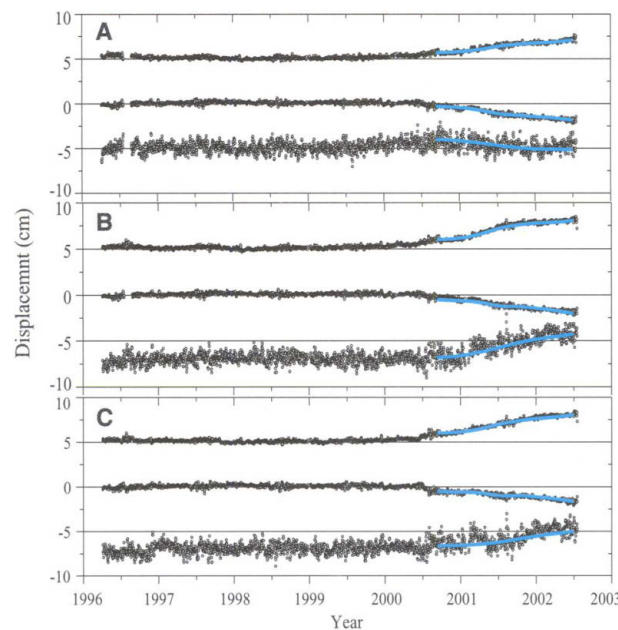


Fig. 2. Detrended time series of east-west (top), north-south (middle), and up-down (bottom) displacements at selected GPS stations [(A) 303, (B) 054, (C) 096] denoted by open circles in Fig. 1B. East, north, and up are positive. Zero slant in these figures means that ground motion is reduced to the steady state deformation in Fig. 1B. The selected stations show clear deviated motion from 2001 onwards. The blue lines indicate computed values from the estimated model.

REPORTS

release rate from July 2001 (fig. S2). Cumulative moment amounts to the equivalent of an $M_w = 6.7$ earthquake in June 2002.

The computed ground displacements (Figs. 2 and 3) from the estimated slip model are consistent with the observed displacements. A notable discrepancy is observed in the Boso peninsula, where observed eastward crustal motion is not consistent with the model (Fig. 3).

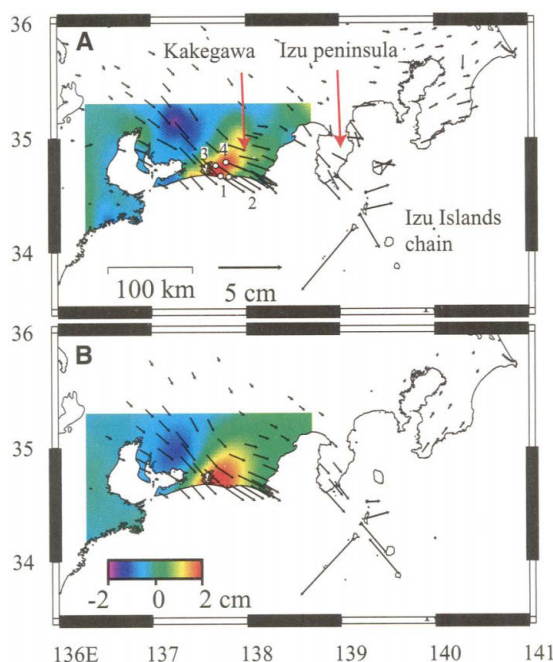
Previous studies of silent earthquakes suggest a tendency for aseismic slips to occur in weakly coupled regions (8, 15, 16), such as the western Tokai region. Re-examination of the past baseline measurements by electromagnetic distance meter suggests a possibil-

ity of at least two similar silent events near the area of the event of 2001 during the periods 1978–83 and 1987–91 (17, 18). Though the past two silent events in the western Tokai region did not lead to a catastrophic rupture, we do not know whether the 2001 silent earthquake will eventually subside or lead to a catastrophic event. However, one thing is clear: the current aseismic slip in the western Tokai is changing stress state such that it is favorable for the Tokai earthquake with the Coulomb failure stress change (ΔCFS), estimated at about 5 kilopascal (kPa) near Cape Omaezaki (Fig. 4) in the Tokai earthquake source area in June 2002, assuming rigidity of 30 gigapascal (GPa), Poisson's

ratio of 0.25, and friction coefficient of 0.2 (19).

The detection of the 2001 silent event supports the hypothesis of a silent event as the cause of the upheavals in the Kakegawa (Fig. 3) (inland of the Tokai region), detected by leveling several days before the 1944 Tonankai earthquake (3), because the present aseismic slip area is close to the assumed silent event in 1944 (20) and because both events caused uplift in Kakegawa (Fig. 3). The 2000 Izu Islands event may have triggered the aseismic slip in the Tokai region, though estimated ΔCFS of ~ 0.5 kPa near Lake Hamana in the western Tokai is very small ordinarily (19).

Fig. 3. (A) Solid arrows represent detrended crustal deformation or anomaly from the steady deformation in Fig. 1B for the period between January 2001 and June 2002. Open circles numbered 1, 2, 3, and 4 represent 054, 098, 097, and 096 stations, respectively. Southeastward motion in the Tokai region suggests occurrence of a slow earthquake. Color represents observed vertical anomaly motion from the steady state for the same period. Northeast-southwest trending uplift area is observed east of Lake Hamana with the maximum of about 2 cm. (B) Computed crustal deformation for the same period from the estimated model in this study.



References and Notes

1. N. Inouchi, H. Sato, *Bull. Geogr. Surv. Inst. Jpn.* **21**, 10 (1975).
2. K. Ishibashi, in *Earthquake Prediction*, vol. 4 of *Maurice Ewing Series*, D. W. Simpson, P. G. Richards, Eds. (American Geophysical Union, Washington, DC, 1981), pp. 297–332.
3. K. Mogi, in *Earthquake Prediction*, vol. 4 of *Maurice Ewing Series*, D. W. Simpson, P. G. Richards, Eds. (American Geophysical Union, Washington, DC, 1981), pp. 43–51.
4. T. Sagiya, *Geophys. Res. Lett.* **26**, 2315 (1999).
5. T. Nishimura et al., *Geophys. Res. Lett.* **28**, 3745 (2001).
6. S. Sakai et al., *Geol. Mag.* **110**, 145 (2001).
7. Materials and methods area available as supporting material on Science Online.
8. S. Ozawa, M. Murakami, T. Tada, *J. Geophys. Res.* **106**, 787 (2001).
9. We do Kalman filtering twice adopting the state vector $x_{n|n} = (u, v)$, where u and v are fault slip and slip velocity. The initial state is $x_{0|0} = (v_0, t, v_0)$ ($t = 0$), where t indicates time. v_0 is estimated in the first filtering. Observational probability at time n is computed under normalized space-time smoothness prior (27) which is derived from applying spatial smoothing of velocity for predicted $x_{n|n-1}$. The product of these observational probabilities for the entire period is a conditional total observation probability under the initial state, in which v_0 has a prior distribution $Z \exp[-\alpha^2 v_0^T G v_0]$, where Z , α , and G represent a nor-

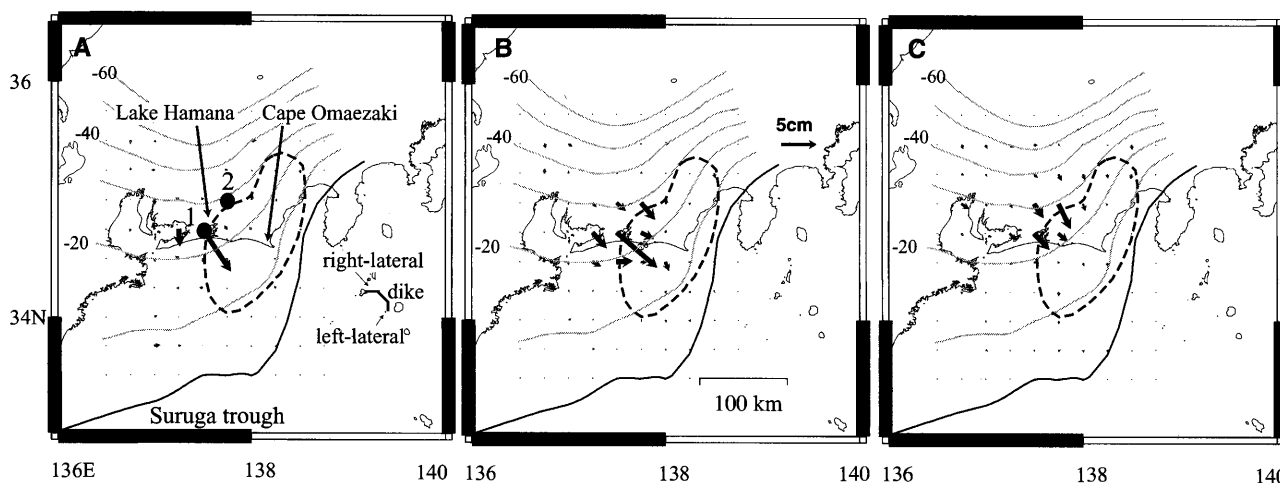


Fig. 4. Estimated time evolution of interplate slip in the Tokai region. Solid arrows represent aseismic slip of the Eurasian plate against the Philippine Sea plate. 1 standard deviation is estimated at about 1 cm. Dashed line indicates the estimated source area of the anticipated Tokai earthquake. Gray solid lines represent isodepth contours of the plate boundary estimated by Ishida (13) in km. Data from (A) 2000.69–

2001.25 (Universal time–Japan time), (B) 2001.77–2002.41 years (in universal time), and (C) 2001.25–2001.77, and (C) 2001.77–2002.41 years (in universal time). Solid dots numbered 1 and 2 [in (A)] show locations of two representative points where modeled interplate slip is plotted in fig. S1. Solid lines denoted by “right-lateral,” “dike,” and “left-lateral” in the Izu Islands [in (A)] represent right-lateral dike, and left-lateral faults of the adopted Izu Islands model (12).

malization factor, a spatial smoothing parameter for slip velocity, and smoothness matrix (8). The log likelihood is approximately computed by adding $\log[Z \int \exp[-(v_0 - \hat{v}_0)^T V_0^{-1} (v_0 - \hat{v}_0)] dv_0]$, where \hat{v}_0 and V_0 are estimated v_0 and its covariance in the first filtering, to logarithm of the above conditional probability with $-\alpha^2 \hat{v}_0^T G \hat{v}_0$ in the second filtering, since $Z \exp[-\alpha^2 \hat{v}_0^T G \hat{v}_0] \times$ (conditional probability) $\propto \exp[-(v_0 - \hat{v}_0)^T V_0^{-1} (v_0 - \hat{v}_0)]$.

10. P. Segall, M. Matthews, *J. Geophys. Res.* **102**, 22391 (1997).
11. J. J. McGuire, P. Segall, M. Miyazaki, *Eos* **82**, F265 (2001).
12. On the basis of Nishimura *et al.* (5), we estimate rectangular fault parameters of the Izu Islands model comprising dike, right-lateral and left-lateral faults (Fig. 4) by linear least squares fitting, using Okada's formula (22). Because of the sparsely distributed GPS sites in the Izu Islands compared with the Tokai region, we constrain the final state of the Izu Islands

model incorporating the estimated slip distribution on the above rectangular faults by Yabuki and Matsuura's method (23) to the total anomaly data for the entire period. We considered that the final state of the Izu Islands model is not so different from the solution by Yabuki and Matsuura's method. We also constrain that rake angle is within 0 ± 45 for the right-lateral and left-lateral faults with unidirectional motion (17) over time for all the components including dike opening.

13. M. Ishida, *J. Geophys. Res.* **97**, 489 (1992).
14. S. Matsumura, *Tectonophysics* **273**, 271 (1997).
15. H. Hirose, K. Hirahara, F. Kimata, N. Fujii, S. Miyazaki, *Geophys. Res. Lett.* **26**, 3237 (1999).
16. I. Hirose, I. Kawasaki, Y. Okada, T. Sagiya, Y. Tamura, *J. Seismol. Soc. Jpn.* **53**, 11 (2000).
17. F. Kimata, K. Hirahara, N. Fujii, H. Hirose, *Eos* **82**, F266 (2001).
18. T. Sagiya, *Eos* **82**, F1265 (2001).
19. R. Harris, *J. Geophys. Res.* **103**, 24347 (1998).

20. A. T. Linde, I. S. Sacks, *Eos* **78**, F156 (1997).
21. Y. Fukahata, A. Nishitani, M. Matsuura, in preparation.
22. Y. Okada, Y., *Bull. Seismol. Soc. Am.* **75**, 1135 (1985).
23. T. Yabuki, M. Matsuura, *Geophys. J. Int.* **109**, 363 (1992).
24. We are grateful to S. Miyazaki of the Earthquake Research Institute, University of Tokyo, and J. J. McGuire and P. Segall of Stanford University for their explanation about their latest time-dependent inversion study.

Supporting Online Material
www.sciencemag.org/cgi/content/full/1076780/DC1
 Materials and Methods
 Figs. S1 and S2

30 July 2002; accepted 24 September 2002
 Published online 3 October 2002;
 10.1126/science.1076780
 Include this information when citing this paper.

Stronger Constraints on the Anthropogenic Indirect Aerosol Effect

Ulrike Lohmann* and Glen Lesins

The anthropogenic indirect aerosol effects of modifying cloud albedo and cloud lifetime cannot be deduced from observations alone but require a modeling component. Here we validate a climate model, with and without indirect aerosol effects, by using satellite observations. The model agrees better with observations when both indirect aerosol effects are included. However, the simulated clouds are more susceptible to aerosols than the observed clouds from the POLDER satellite, thus overestimating the indirect aerosol effect. By taking the difference in susceptibilities into account, the global mean total anthropogenic aerosol effect is reduced from -1.4 to -0.85 watts per square meter.

The anthropogenic component of sulfate and carbonaceous aerosols has substantially increased the global mean aerosol burden from preindustrial times to the present and can influence climate in different ways. The direct aerosol effect is caused by the absorption and scattering of solar radiation. Additionally, aerosols exert an indirect effect by acting as cloud condensation nuclei, thereby affecting the initial cloud droplet number concentration (CDNC), albedo, precipitation formation, and lifetime of warm clouds. For a constant liquid water path, a higher cloud droplet number causes an increase in cloud albedo (cloud albedo effect). Reductions in precipitation efficiency due to more but smaller cloud droplets slow down precipitation formation and increase cloud lifetime (cloud lifetime effect). The cooling from both indirect effects has been estimated by climate models to be -1 to -4.4 W m⁻² in the global mean (1-5), but this estimate is still very

poorly constrained and is an important source of uncertainty in projections of future climate change (6, 7).

Data from a regional chemical transport model, together with satellite data estimating the cloud albedo effect in the North Atlantic, show that the cloud-top spherical albedo was enhanced over two-week episodes by 0.02 to 0.15 for the same liquid water path distribution (8) relative to the unperturbed case. POLDER satellite data were used (9) to derive aerosol concentration and cloud droplet effective radii (CDR) from 8 months of space-borne measurements and to explore the effect of aerosols on cloud microphysics. It was found that the cloud droplet size decreases with increasing aerosol index (AI) (10), which is representative of the aerosol column number concentration, indicating that the effect of aerosols on cloud microphysics is significant and occurs on a global scale. However, these data alone are not sufficient to quantify the magnitude of the global indirect aerosol effects between preindustrial times and present day.

From historical climate record data of oceanic and atmospheric warming together with ensembles of simulations with one

climate model of reduced complexity, the anthropogenic indirect aerosol effects have recently been constrained within the range of 0 to -1.2 W m⁻² (11). Here, a complex global climate model rather than a simple climate model is used to try to determine the importance of the cloud albedo and the cloud lifetime effects by finding the model configurations that produce results that most resemble the observational data (9) in order to estimate the anthropogenic aerosol effects constrained by POLDER data.

We used the ECHAM4 general circulation model (GCM) (12) in T30 horizontal resolution to estimate the anthropogenic aerosol effect on a global scale. The GCM includes a fully coupled aerosol-cloud microphysics module (3, 13, 14). The reference simulation, ECHAM-CTL, includes both indirect aerosol effects with the use of present-day emissions (15). To turn off the cloud albedo effect (simulation ECHAM-2ND-AIE), we prescribed CDNC everywhere as a function of height in the radiation calculation: CDNC equals 150 cm⁻³ near the surface and decreases to 50 cm⁻³ in the midtroposphere. In the simulation ECHAM-NO-AIE, a constant number of cloud droplets was used in the cloud microphysics and the radiation calculations (16). We also ran a preindustrial climate simulation, ECHAM-PI, in which the sulfate and carbonaceous (black carbon and organic carbon) aerosols from fossil fuel and biomass burning were set to zero (17), leaving natural emissions from forests as the only source for organic carbon, and dimethyl sulfide emissions from the ocean and volcanoes as the only sources for sulfate aerosols.

Figure 1 shows AI as obtained from the control simulation as well as the difference between ECHAM's AI and that obtained from POLDER and averaged over March, April, and May 1997 (9, 18, 19). We calculated AI offline with the use of Mie theory, assuming an externally mixed aerosol (20). ECHAM correctly simulates a large land-sea contrast in AI, with the larger AI over land resulting from pollution as observed from

Department of Physics and Atmospheric Science, Dalhousie University, Halifax, Nova Scotia B3H 3J5, Canada.

*To whom correspondence should be addressed. E-mail: Ulrike.Lohmann@Dal.ca